The Astrophysical Journal Letters, 881:L19 (11pp), 2019 August 10 https://doi.org/10.3847/2041-8213/ab322d

TESS Spots a Compact System of Super-Earths around the Naked-eye Star HR 858

Andrew Vanderburg[1,27], Chelsea X. Huang[2,28], Joseph E. Rodriguez[3,29], Juliette C. Becker[4,30,31], George R. Ricker[2], Roland K. Vanderspek[2], David W. Latham[3], Sara Seager[2,5], Joshua N. Winn[6], Jon M. Jenkins[7], Brett Addison[8], Allyson Bieryla[3], Cesar Briceño[9], Brendan P. Bowler[1], Timothy M. Brown[10,11], Christopher J. Burke[2], Jennifer A. Burt[2,28], Douglas A. Caldwell[7,12], Jake T. Clark[8], Ian Crossfield[2], Jason A. Dittmann[5,32], Scott Dynes[2], Benjamin J. Fulton[13], Natalia Guerrero[2], Daniel Harbeck[11], Jonathan Horner[8], Stephen R. Kane[14], John Kielkopf[15], Adam L. Kraus[1], Laura Kreidberg[3,33], Nicolas Law[16], Andrew W. Mann[16], Matthew W. Mengel[8], Timothy D. Morton[17,18], Jack Okumura[8], Logan A. Pearce[1], Peter Plavchan[19], Samuel N. Quinn[3], Markus Rabus[11,20], Mark E. Rose[7], Pam Rowden[21], Avi Shporer[2], Robert J. Siverd[22], Jeffrey C. Smith[7,12], Keivan Stassun[22,23], C. G. Tinney[24], Rob Wittenmyer[8], Duncan J. Wright[8], Hui Zhang[25], George Zhou[3,34], and Carl A. Ziegler[26]

[1] Department of Astronomy, The University of Texas at Austin, Austin, TX 78712, USA
[2] Department of Physics, and Kavli Institute for Astrophysics and Space Research, Massachusetts Institute of Technology, Cambridge, MA 02139, USA
[3] Center for Astrophysics | Harvard and Smithsonian, Cambridge, MA 02138, USA
[4] Department of Astronomy, University of Michigan, Ann Arbor, MI 48109, USA
[5] Department of Earth and Planetary Sciences, MIT, 77 Massachusetts Avenue, Cambridge, MA 02139, USA
[6] Department of Astrophysical Sciences, Princeton University, 4 Ivy Lane, Princeton, NJ 08544, USA
[7] NASA Ames Research Center, Moffett Field, CA 94035, USA
[8] Centre for Astrophysics, University of Southern Queensland, Toowoomba, QLD 4350, Australia
[9] Cerro Tololo Inter-American Observatory, Casilla 603, La Serena, Chile
[10] University of Colorado/CASA, Boulder, CO 80309, USA
[11] Las Cumbres Observatory Global Telescope Network, Santa Barbara, CA 93117, USA
[12] SETI Institute, Mountain View, CA 94043, USA
[13] Caltech/IPAC-NExScI, 1200 East California Boulevard, Pasadena, CA 91125, USA
[14] Department of Earth and Planetary Sciences, University of California, Riverside, CA 92521, USA
[15] Department of Physics and Astronomy, University of Louisville, Louisville, KY 40292, USA
[16] Department of Physics and Astronomy, University of North Carolina at Chapel Hill, Chapel Hill, NC 27599, USA
[17] Department of Astronomy, University of Florida, Gainesville, FL, 32611, USA
[18] Center for Computational Astrophysics, Flatiron Institute, 162 5th Avenue, New York, NY 10010, USA
[19] George Mason University, Fairfax, VA 22030, USA
[20] Department of Physics, University of California, Santa Barbara, CA 93106-9530, USA
[21] School of Physical Sciences, The Open University, Milton Keynes MK7 6AA, UK
[22] Department of Physics and Astronomy, Vanderbilt University, Nashville, TN 37235 USA
[23] Department of Physics, Fisk University, Nashville, TN 37208, USA
[24] Exoplanetary Science at UNSW, School of Physics, UNSW, Sydney, NSW 2052, Australia
[25] School of Astronomy and Space Science, Key Laboratory of Modern Astronomy and Astrophysics in Ministry of Education, Nanjing University, Nanjing 210046, Jiangsu, People's Republic of China
[26] Dunlap Institute for Astronomy and Astrophysics, University of Toronto, Toronto, ON M5S 3H4, Canada
Received 2019 May 7; revised 2019 July 11; accepted 2019 July 12; published 2019 August 9

Abstract

Transiting Exoplanet Survey Satellite (*TESS*) observations have revealed a compact multiplanet system around the sixth-magnitude star HR 858 (TIC 178155732, TOI 396), located 32 pc away. Three planets, each about twice the size of Earth, transit this slightly evolved, late F-type star, which is also a member of a visual binary. Two of the planets may be in mean motion resonance. We analyze the *TESS* observations, using novel methods to model and remove instrumental systematic errors, and combine these data with follow-up observations taken from a suite of ground-based telescopes to characterize the planetary system. The HR 858 planets are enticing targets for precise radial velocity observations, secondary eclipse spectroscopy, and measurements of the Rossiter–McLaughlin effect.

Key words: planetary systems – planets and satellites: detection – stars: individual (HR 858, TIC 178155732)

Supporting material: data behind figure

1. Introduction

The *Kepler space telescope* was history's most prolific exoplanet-detecting tool (Borucki et al. 2010). During its primary and extended *K2* missions (Howell et al. 2014), *Kepler* searched over 500,000 stars across 5% of the sky for small, periodic dimming events caused by transiting planets. *Kepler*'s survey revealed a stunning diversity of planets in terms of size (Fressin et al. 2013), architecture (Lissauer et al. 2011), and environment (Mann et al. 2017), but due to the survey's design, most of *Kepler*'s discoveries orbit faint and otherwise anonymous stars hundreds or thousands of parsecs from Earth. Follow-up studies to characterize *Kepler*'s planets and investigate their detailed properties are limited by the host stars' faint apparent magnitudes.

[27] NASA Sagan Fellow.
[28] Juan Carlos Torres Fellow.
[29] Future Faculty Leaders Fellow.
[30] NSF Graduate Research Fellow.
[31] Leinweber Center for Theoretical Physics Graduate Fellow.
[32] 51 Pegasi b Postdoctoral Fellow.
[33] Harvard Junior Fellow.
[34] NASA Hubble Fellow.

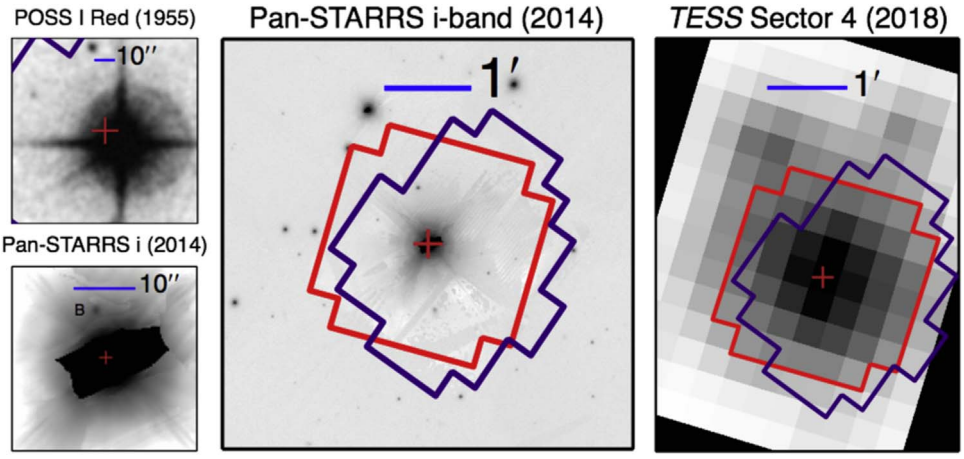

Figure 1. Images of the field surrounding HR 858. Top left: from the first Palomar Observatory Sky Survey, obtained with a red-sensitive photographic emulsion in 1955. The red cross is the current position of HR 858. Bottom left: from the Pan-STARRS survey obtained with an *i*-band filter in 2014. The faint comoving companion HR 858 B is marked to the north of HR 858. Middle: from the Pan-STARRS survey, over a wider field of view, obtained with an *i*-band filter in 2014. Purple and red lines mark the boundary of the *TESS* photometric apertures for Sectors 3 and 4, respectively. Right: summed *TESS* image. North is up and east is to the left in all the images.

Now, the recently commissioned *Transiting Exoplanet Survey Satellite* (*TESS*; Ricker et al. 2015) is beginning to identify analogs of the systems discovered by *Kepler*, but around the nearest and brightest stars in the sky. Using four wide-angle cameras, *TESS* is searching 80% of the sky for transiting exoplanets during its two-year primary mission. Already, *TESS* has discovered several new exoplanets around bright stars that are well suited for follow-up observations (Huang et al. 2018a; Vanderspek et al. 2019), and hundreds more *TESS* planet candidates await confirmation.[35]

Early in the mission, most *TESS* planet discoveries were singly transiting systems (Nielsen et al. 2019; Rodriguez et al. 2019; Wang et al. 2019), but now that some stars have been observed for longer time baselines, the survey is detecting transiting systems with increasingly complex architectures (Dragomir et al. 2019; Quinn et al. 2019). Here, we report the discovery of three super-Earths around the naked-eye star HR 858. The planets are all about twice the size of Earth and have periods of 3.59, 5.98, and 11.23 days. HR 858 b and c orbit within 0.03% of the 3:5 period ratio, and may be in true mean motion resonance. This compact and near-resonant architecture harkens back to the systems of tightly packed inner planets discovered by *Kepler*, but HR 858 is hundreds to thousands of times brighter ($V = 6.4$) than the hosts of those *Kepler* systems. We describe our observations in Section 2, our analysis to determine system parameters in Section 3, and our efforts to show that the planet candidates are not false positives in Section 4. We conclude by discussing the HR 858 system architecture and opportunities for follow-up observations in Section 5.

2. Observations and Data Reduction

2.1. TESS *Photometry*

TESS observed HR 858 during the third and fourth sectors of its two-year-long primary mission, obtaining data from 2018 September 20 UT until 2018 November 14 UT. During Sector 4, *TESS* saved and downlinked images of HR 858 every 2 minutes, standard procedure for the bright, nearby dwarf stars around which *TESS* was specifically designed to discover planets. However, during Sector 3, HR 858 fell only a few pixels from the edge of the field of view, so (as for most of the sky) *TESS* only downlinked coadded images with a more-coarsely sampled 30 minute cadence.

Once the *TESS* data were transmitted to Earth, we processed the data using two different sets of analysis tools in parallel: the MIT Quick Look Pipeline (QLP; C. X. Huang et al. 2019, in preparation) and the Science Processing Operations Center (SPOC; Jenkins 2015; Jenkins et al. 2016) pipeline based at NASA Ames Research Center. After extracting light curves from the *TESS* pixel data and searching for periodic signals, both pipelines identified the signatures of two transiting exoplanet candidates. These signals, which repeated every 3.59 and 5.98 days, were tested using standard diagnostics[36] to determine whether the candidate transits were caused by some astrophysical or instrumental phenomenon other than a genuine system of transiting planets. We found no indication that these signals were false positives, and alerted the community to their existence via the MIT *TESS* Alerts webpage (see footnote 35). We tentatively designated the planet candidates HR 858 b and c.

Next, working from the calibrated pixel files,[37] we re-extracted light curves from a series of both circular and irregularly shaped apertures (Vanderburg et al. 2016). We ultimately chose the apertures shown in Figure 1, which minimized photometric scatter and contamination from two nearby stars. Systematic errors are present in the light curves from both sectors. Unlike *Kepler*, whose instrumental systematics were dominated by changes in the spacecraft's focus (Jenkins et al. 2010), and *K2*, whose instrumental systematics were dominated by pointing drifts on timescales longer than single exposures (Vanderburg & Johnson 2014), *TESS*'s instrumental systematics are dominated by pointing jitter on timescales shorter than an exposure. Figure 2 shows common

[35] https://tev.mit.edu/

[36] These tests included searches for shallow secondary eclipses, differences in transit depth between even and odd-numbered transits, and shifts in HR 858's apparent position during transit.

[37] We used a cutout from the online TESScut (https://mast.stsci.edu/tesscut/) tool for Sector 3 and the calibrated 2 minute cadence target pixel files for Sector 4.

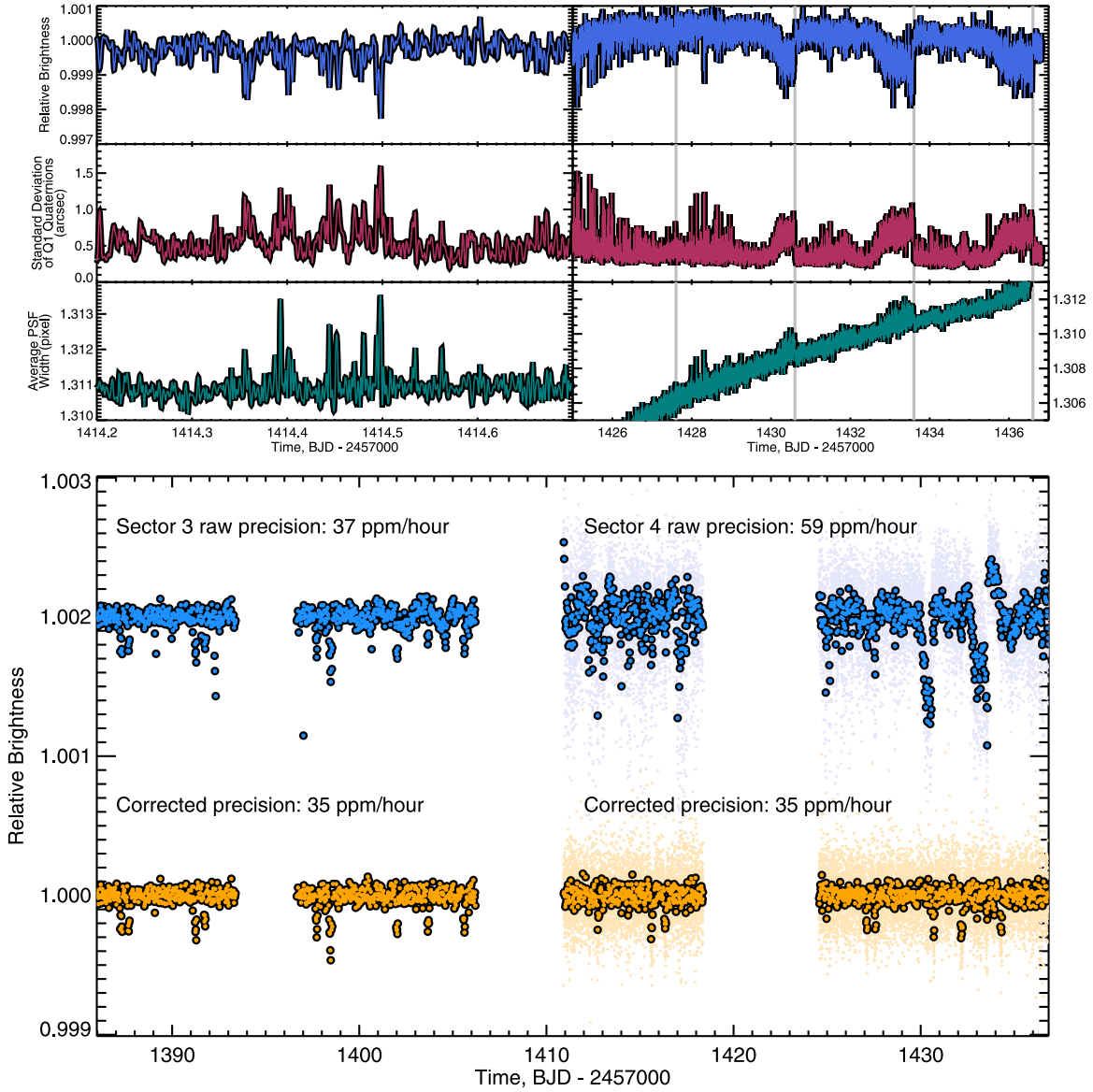

Figure 2. Systematic errors in the Sector 4 *TESS* light curve of HR 858. Top panels: time series of measured brightness (top row), standard deviation of the Q1 quaternion component within each 2 minute science exposure (middle row), and best-fit width of the *TESS* PSF (bottom row). The time ranges shown in the two columns differ to emphasize the varying nature of the short- and long-timescale systematics. Times when the spacecraft underwent reaction wheel momentum dumps are shown as vertical gray lines. Note that the time series of PSF width shows a slow drift due to focus change after a spacecraft anomaly caused an onboard heater to activate. Bottom: *TESS* light curves of HR 858 before (blue) and after (orange) removal of systematic errors as described in Section 2.1. Faint points are individual 2 minute exposures, and bold points are averages in 30 minute bins. The photometric precision is estimated by binning the light curve to one-hour exposures and calculating the point-to-point scatter.

features appearing in the HR 858 light curve, the width of the *TESS* point-spread function (PSF; from a fit of the *TESS* images to a 2D Gaussian), and the intra-exposure scatter in engineering "quaternion" data.[38] These systematics are present on both short (exposure to exposure) and long (∼day) timescales (which come from steady increases in the pointing scatter ahead of reaction wheel momentum dump events).

We performed our own correction for the *TESS* systematics. First, we ignored data where the SPOC quality flag was nonzero and during the following time intervals (where $t \equiv$ BJD − 2,457,000): $t < 1385.96$ (while the *TESS* operations team conducted tests on the spacecraft's attitude control system), $1393.4 < t < 1396.6361$, $1406.25 < t < 1410.9054$, and $1423.5136 < t < 1424.5539$ (near *TESS*'s orbital perigee when earthshine contaminated the aperture), and $1418.4915 < t < 1423.5136$ (when spacecraft/instrument communications were interrupted, shutting down the instrument, activating a heater, and introducing systematic trends).

We then treated the remaining short- and long-timescale systematic behavior separately. The long-timescale behavior gives rise to slow trends in the light curve with jumps each time the spacecraft resets the reaction wheel speeds by briefly firing

[38] The quaternion measurements are 2 s cadence vector time series that describe the spacecraft attitude based on observations of a set of guide stars. For each vector component (Q1, Q2, Q3), we take the standard deviation of all measurements within each 2 minute science image. The quaternions are measured in each *TESS* camera (in camera coordinates along the CCD row, column, and roll about the boresight), and are rotated into spacecraft coordinates (where the roll axis is pointing at the sky between Cameras 2 and 3). The quaternions are available online at https://archive.stsci.edu/missions/tess/engineering/.

its thrusters (a "momentum dump"). We remove this behavior by fitting a basis spline (with robust outlier rejection and knots spaced roughly every 1.5 days) to the light curve and introducing discontinuities in the basis spline at the time of each momentum dump. Dividing this spline fit from the light curve effectively removes the long-timescale drifts.

We treated the short-timescale behavior in the *TESS* light curves differently between Sector 3 and Sector 4. During Sector 3, there are only a handful of exposures strongly affected by short-timescale pointing jitter. We simply exclude the 2% of points with the widest measured PSF (indicating the largest intra-exposure pointing scatter), after removing slow drifts in the PSF width time series as done for the light curves (introducing discontinuities at momentum dumps). This cut corresponds roughly to excluding points with PSF width 7.5σ larger than the high-pass-filtered median width, and removes all noticeable flux outliers from the light curve. This strategy is similar to that of Fausnaugh et al. (2019), who identified and removed anomalous points using the mean and standard deviation of the quaternion time series within exposures.

The short-timescale systematic effects in the Sector 4 light curve were higher amplitude and more pervasive, so instead of simply clipping strongly affected points from the time series, we opted to decorrelate the light curve against other time series. In Sector 4, instead of using the PSF width as a proxy for spacecraft motion, we worked with the less-noisy quaternion data,[39] with long-term trends removed as done for the light curves and PSF width time series. We performed the decorrelation using a matrix-inversion least-squares technique, iteratively removing 3σ outliers from the fit until convergence. We experimented with decorrelating the light curve against different combinations of parameters including the averages and standard deviations of the (Q1, Q2, Q3) quaternions within each exposure, averages and standard deviations of products of quaternions (Q1 × Q2, Q2 × Q3, Q1 × Q3), and various cotrending basis vectors used by the SPOC pipeline's Presearch Data Conditioning (PDC) module (Smith et al. 2012; Stumpe et al. 2014). We also experimented with decorrelating against higher (quadratic and cubic) orders of these time series. In the end, we found best results by decorrelating only against the standard deviation of the Q1 and Q2 quaternions and the seven cotrending vectors from PDC's band 3 (fast timescale) correction. The result of this decorrelation (and the long-timescale correction) on the Sector 4 *TESS* data is shown in the bottom panel of Figure 2.

After producing light curves with systematic effects removed, we re-searched the light curve to look for additional transiting planet candidates. We searched the combined two-sector light curve (after binning the Sector 4 light curve to 30 minute cadence) with a Box-Least-Squares pipeline (Kovács et al. 2002; Vanderburg et al. 2016). In addition to recovering the two candidates identified by the QLP and SPOC pipelines, we detected a third convincing transit signal with a period of 11.23 days. *TESS* detected three transits of this candidate: two in Sector 3, and one in Sector 4. After identifying the new candidate, we re-derived the systematics correction while excluding points taken during transits of all three planet candidates, and used this light curve in our analysis.

[39] We used the quaternions derived from Camera 2 (where HR 858 was observed) in camera coordinates. We converted the quaternion timestamps from spacecraft time to barycentric Julian date (BJD) toward HR 858.

We measured the centroid position of HR 858 in each *TESS* image and converted the measurements to time series in R.A. and decl. The average changes in the position of HR 858's centroid during each planet candidate's transits were consistent with zero (with a precision of a few milliarcseconds). This confidently rules out the possibility that any star more than 40″ away is the true source of the dimming events.

2.2. Archival and High-resolution Imaging

We examined the region of sky around HR 858 using archival surveys and newly obtained data (Figure 1). Archival imaging from the Palomar Observatory Sky Survey (POSS) rules out background stars within about 6.5 mag[40] of HR 858's brightness at its present-day position, while images from the Pan-STARRS telescope identify seven stars besides HR 858 inside the TESS photometric apertures. All of these stars are at least 9 mag fainter than HR 858, and six of the seven are likely background objects. Parallax and proper motions observations from *Gaia* DR2 (Gaia Collaboration et al. 2016, 2018) reveal that the nearest star to HR 858 (about 8.″4 to the northeast) is a comoving companion (270 au projected separation). The sky-projected velocity of HR 858 and the companion differ by only $2.108 \pm 0.034\,\mathrm{km\,s^{-1}}$, consistent with a bound orbit, and analysis of the companion's spectral energy distribution (SED; following Stassun et al. 2018) reveals it to be an M-dwarf with $T_{\rm eff} = 2800 \pm 300\,\mathrm{K}$ and $R_\star = 0.17 \pm 0.04\,R_\odot$. The *Gaia* observations of the comoving companion show large astrometric scatter; this may be due to systematic effects from the nearby, much brighter primary star, or it may be an indication that the comoving companion is itself an unresolved binary (Evans 2018; Rizzuto et al. 2018). Some basic information about the comoving companion, which we call HR 858 B, is given in Table 2.

We also obtained a high-resolution *I*-band image of HR 858 with the HRCam speckle imager on the Southern Astrophysical Research (SOAR) telescope. The observations and analysis were conducted as described by Tokovinin (2018). Our observation was sensitive to nearly equal-brightness companions at separations of 0.″06 (1.8 au projected distance) and fainter stars up to seven magnitudes fainter than HR 858 at larger (3.″15, 100 au projected) separations. We detected no additional stars brighter than these contrast limits near HR 858.

2.3. High-resolution Spectroscopy

We obtained high-resolution reconnaissance spectroscopy of HR 858 to determine spectroscopic parameters and rule out large radial velocity (RV) variations. We observed HR 858 twice with the Tillinghast Reflector Echelle Spectrograph (TRES[41]) on the 1.5 m telescope at Fred L. Whipple Observatory, once with the CHIRON spectrograph on the 1.5 m SMARTS telescope at Cerro Tololo Inter-American Observatory (CTIO), once with the echelle spectrograph on the 2.3 m Australian National University (ANU) telescope at Siding Spring Observatory, and seven times with the Network of Robotic Echelle Spectrographs (NRES; Eastman et al. 2014; Siverd et al. 2016, 2018) operated by Las Cumbres Observatory (LCO; Brown et al. 2013) from CTIO and South African Astronomical Observatory (SAAO). The reconnaissance observations showed no

[40] Based on the lack of a visible bulge in HR 858's saturated PSF and the size of the saturated PSFs of nearby 12th–13th magnitude stars.

[41] www.sao.arizona.edu/html/FLWO/60/TRES/GABORthesis.pdf

large RV variations or evidence for a composite spectrum. From the TRES data, we measured an absolute RV of $9.6 \pm 0.1\,\mathrm{km\,s^{-1}}$ by cross-correlating the observed spectra with synthetic spectra derived from Kurucz (1992) atmosphere models and applying empirical corrections to shift the measured velocity to the IAU scale (Stefanik et al. 1999). We found no evidence for large ($\sim$km s^{-1}) RV variations that might indicate HR 858 is a close binary star. The measured absolute velocity is consistent with archival RV measurements going back over a decade from the *Gaia* mission (Gaia Collaboration et al. 2018), Pulkuvo Observatory (Gontcharov 2006), and the Geneva Copenhagen Survey (Casagrande et al. 2011).

After our initial reconnaissance, we obtained 30 observations on 13 separate nights with the MINERVA-Australis telescope array at Mt. Kent Observatory in Queensland, Australia (Addison et al. 2019) to place stronger limits on the transiting companions' masses. We measured RVs via least-squares analysis (Anglada-Escudé & Butler 2012) and corrected for spectrograph drifts with simultaneous Thorium Argon arc lamp observations. From these data, which showed scatter of about $14\,\mathrm{m\,s^{-1}}$, we calculate upper limits (95% confidence) on the masses of the three planet candidates around HR 858 of about $45\,M_\oplus$ each using the RadVel package (Fulton et al. 2018). Our RV observations are summarized in Table 1.

We determined spectroscopic parameters from the TRES spectra using the Stellar Parameter Classification (SPC) code (Buchhave et al. 2012, 2014) and found parameters ($T_{\rm eff} = 6201 \pm 50$, $\log g_{\rm cgs} = 4.19 \pm 0.10$, $[\mathrm{m/H}] = -0.14 \pm 0.08$)[42] consistent with literature determinations (Gray et al. 2006; Casagrande et al. 2011). Our spectroscopic reconnaissance also found that HR 858 is rotating moderately rapidly. Following Zhou et al. (2018), we measured a projected rotational velocity of $v \sin i = 8.3 \pm 0.5\,\mathrm{km\,s^{-1}}$ and a macroturbulent velocity of $v_{\rm mac} = 5.2 \pm 0.5\,\mathrm{km\,s^{-1}}$. An analysis of the NRES spectra using SpecMatch (Petigura 2015; Petigura et al. 2017) yielded results ($T_{\rm eff} = 6199 \pm 100$, $\log g_{\rm cgs} = 4.3 \pm 0.1$, $[\mathrm{m/H}] = -0.10 \pm 0.07$) consistent with those from TRES and SPC.

3. Determination of System Parameters

We determined system parameters using the EXOFASTv2 global modeling software (Eastman et al. 2013; Eastman 2017). EXOFASTv2 uses Markov Chain Monte Carlo (MCMC) to explore a high-dimensional space in physical model parameters and determine best-fit values and uncertainties. We fit the two-sector *TESS* light curve and an SED constructed from archival broadband photometry (listed in Table 2). We imposed priors on spectroscopic parameters from TRES and the *Gaia* parallax, and we enforced an upper limit on *V*-band extinction of $A_v < 0.04898$ mag from Schlegel et al. (1998). MIST isochrones (Choi et al. 2016) were used to constrain the stellar parameters. Each MCMC link's linear and quadratic limb-darkening parameters were assigned by interpolating from Claret & Bloemen (2011) models at that link's surface gravity, effective temperature, and metallicity. We ran the fit until convergence (defined as 1000 independent posterior draws after the chains all reached a Gelman–Rubin statistic less than 1.01). The results of our fit are given in Table 2, and the TESS light curve is shown with our best-fit transit model in Figure 3.

[42] [m/H] is the star's overall metallicity assuming HR 858's metals have the same relative proportions as in the Sun.

Table 1
Summary of Radial Velocity Observations

Time BJD	RV (km s^{-1})	RV Error (km s^{-1})	Instrument
2458508.627	9.5450	0.1000	TRES
2458510.649	9.5990	0.1000	TRES
2458536.892	9.3000	0.5000	ANU
2458532.543	8.1940	0.0140	CHIRON
2458523.008	9.7820	0.0051	MINERVA-Australis
2458523.016	9.7860	0.0049	MINERVA-Australis
2458524.913	9.7892	0.0058	MINERVA-Australis
2458524.927	9.7811	0.0058	MINERVA-Australis
2458524.943	9.7773	0.0058	MINERVA-Australis
2458524.957	9.7319	0.0056	MINERVA-Australis
2458524.972	9.7726	0.0055	MINERVA-Australis
2458526.974	9.8016	0.0058	MINERVA-Australis
2458526.985	9.7963	0.0057	MINERVA-Australis
2458528.948	9.7806	0.0046	MINERVA-Australis
2458528.956	9.7688	0.0047	MINERVA-Australis
2458528.964	9.7639	0.0047	MINERVA-Australis
2458529.945	9.7676	0.0055	MINERVA-Australis
2458529.952	9.7885	0.0056	MINERVA-Australis
2458529.960	9.7886	0.0056	MINERVA-Australis
2458530.943	9.7718	0.0054	MINERVA-Australis
2458530.950	9.7779	0.0052	MINERVA-Australis
2458531.943	9.7683	0.0051	MINERVA-Australis
2458531.957	9.7761	0.0052	MINERVA-Australis
2458533.947	9.7950	0.0059	MINERVA-Australis
2458533.954	9.7917	0.0059	MINERVA-Australis
2458535.982	9.8029	0.0057	MINERVA-Australis
2458535.990	9.7817	0.0055	MINERVA-Australis
2458536.940	9.7757	0.0056	MINERVA-Australis
2458536.948	9.7740	0.0056	MINERVA-Australis
2458537.954	9.7717	0.0054	MINERVA-Australis
2458537.962	9.7793	0.0058	MINERVA-Australis
2458538.955	9.7609	0.0048	MINERVA-Australis
2458538.966	9.7682	0.0046	MINERVA-Australis
2458509.048	9.8214	0.0096	MINERVA-Australis
2458522.290	8.9689	0.7386	LCO-SAAO
2458533.266	8.8251	0.2172	LCO-SAAO
2458535.568	9.8806	0.1139	LCO-CTIO
2458536.538	9.8718	0.1457	LCO-CTIO
2458538.555	9.9197	0.1491	LCO-CTIO
2458542.258	9.5613	0.2002	LCO-SAAO
2458546.254	8.7488	0.1880	LCO-SAAO

Note. RVs from each instrument have not been corrected for instrumental offsets onto the same velocity system. Times have been converted to BJD_TDB using routines written by Eastman et al. (2010).

We cross-checked the EXOFASTv2 analysis with other less-comprehensive analyses in parallel. In particular, we fit for light curve and stellar parameters following Huang et al. (2018a), and confirmed that our removal of low frequency variability and long-timescale systematics did not significantly affect the fit parameters. Another transit analysis that did not use constraints from the host star's parameters yielded the duration of transit ingress/egress, t_{12} (or the time between the first and second transit contacts; see Figure 1 of Seager & Mallén-Ornelas 2003), and the total transit duration, t_{14} (from first to fourth contact). We also re-derived stellar parameters using an online interface[43] to fit the effective temperature, *V*-band magnitude, and parallax with Padova models (da Silva

[43] http://stev.oapd.inaf.it/cgi-bin/param_1.3

Table 2
HR 858 System Parameters

Parameter	Units	Values		
Identifying Information				
HR 858, HD 17926, HIP 13363, TIC 178155732, TOI 396				
Gaia DR2 Source ID 5064574720469473792				
R.A.	R.A. (J2000)	02:51:56.25		
Decl.	Decl. (J2000)	−30:48:52.3		
$PM_{R.A.}$	Proper Motion in R.A. (mas yr^{-1})	123.229 ± 0.070		
$PM_{Decl.}$	Proper Motion in decl. (mas yr^{-1})	105.788 ± 0.151		
ϖ	Parallax (mas)	31.256 ± 0.070		
B_T	Tycho *B*-band Magnitude	6.956 ± 0.015		
V_T	Tycho *V*-band Magnitude	6.438 ± 0.010		
J	2MASS *J*-band Magnitude	5.473 ± 0.030		
H	2MASS *H*-band Magnitude	5.225 ± 0.030		
Ks	2MASS *K*-band Magnitude	5.149 ± 0.020		
*W*1	*WISE* Band 1 Magnitude	5.098 ± 0.232		
*W*2	*WISE* Band 2 Magnitude	4.941 ± 0.094		
*W*3	*WISE* Band 3 Magnitude	5.171 ± 0.014		
*W*4	*WISE* Band 4 Magnitude	5.100 ± 0.029		
Identifying Information and Photometric Properties for Comoving Companion HR 858 B				
Gaia DR2 Source ID 5064574724768583168				
R.A.	R.A. (J2000)	02:51:56.41		
Decl.	Decl. (J2000)	−30:48:44.2		
$PM_{R.A.}$	Proper Motion in R.A. (mas yr^{-1})	137.125 ± 0.213		
$PM_{Decl.}$	Proper Motion in decl. (mas yr^{-1})	105.865 ± 0.302		
ϖ	Parallax (mas)	32.301 ± 0.167		
G	*Gaia G*-band Magnitude	16.0464 ± 0.05		
Bp	*Gaia Bp*-band Magnitude	17.0142 ± 0.1		
Rp	*Gaia Rp*-band Magnitude	14.4812 ± 0.1		
i	Pan-STARRS *i*-band Magnitude	14.4611 ± 0.05		
z	Pan-STARRS *z*-band Magnitude	14.1671 ± 0.05		
y	Pan-STARRS *y*-band Magnitude	13.0732 ± 0.08		
Observed Stellar Parameters				
$\log g$	Spectroscopic surface gravity (cgs)	4.19 ± 0.1		
T_{eff}	Effective Temperature (K)	6201 ± 50		
[Fe/H]	Metallicity (dex)	−0.14 ± 0.08		
$v \sin i$	Projected rotational velocity (km s^{-1})	8.3 ± 0.5		
Derived Stellar Parameters				
$M_\star$	Mass ($M_\odot$)	$1.145^{+0.074}_{-0.080}$		
$R_\star$	Radius ($R_\odot$)	$1.310^{+0.024}_{-0.022}$		
$L_\star$	Luminosity ($L_\odot$)	$2.348^{+0.069}_{-0.071}$		
$\rho_\star$	Density (cgs)	$0.717^{+0.064}_{-0.063}$		
$\log g$	Model-derived surface gravity (cgs)	$4.262^{+0.032}_{-0.036}$		
u_1	*TESS*-band linear limb-darkening coeff	0.227 ± 0.034		
u_2	*TESS*-band quadratic limb-darkening coeff	0.295 ± 0.035		
Planetary Parameters		b	c	d
P	Period (days)	3.58599 ± 0.00015	$5.97293^{+0.00060}_{-0.00053}$	$11.2300^{+0.0011}_{-0.0010}$
R_P	Radius ($R_\oplus$)	$2.085^{+0.068}_{-0.064}$	1.939 ± 0.069	$2.164^{+0.086}_{-0.083}$
T_C	Time of conjunction (BJD_{TDB})	$2458409.18969^{+0.00084}_{-0.00083}$	$2458415.6344^{+0.0022}_{-0.0014}$	$2458409.7328^{+0.0020}_{-0.0018}$
a	Semimajor axis (au)	$0.0480^{+0.0010}_{-0.0011}$	$0.0674^{+0.0014}_{-0.0016}$	$0.1027^{+0.0022}_{-0.0025}$
i	Inclination (degrees)	$85.50^{+1.5}_{-0.50}$	86.23 ± 0.26	$87.43^{+0.18}_{-0.19}$
e	Eccentricity (95% Confidence)	<0.30	<0.19	<0.28
T_{eq}	Equilibrium temperature (K)	1572^{+22}_{-19}	1326^{+18}_{-16}	1075^{+15}_{-13}
$R_P/R_\star$	Radius of planet in stellar radii	0.01460 ± 0.00035	$0.01358^{+0.00038}_{-0.00039}$	$0.01514^{+0.00050}_{-0.00049}$
$a/R_\star$	Semimajor axis in stellar radii	$7.87^{+0.23}_{-0.24}$	$11.06^{+0.32}_{-0.34}$	$16.85^{+0.49}_{-0.51}$
$d/R_\star$	Planet/star separation at mid transit	$7.29^{+0.83}_{-1.1}$	$10.88^{+0.64}_{-0.81}$	$15.9^{+1.8}_{-2.3}$

Table 2
(Continued)

Parameter	Units	Values		
δ	Transit depth $(R_p/R_\star)^2$	0.000213 ± 0.000010	0.000184 ± 0.000011	0.000229 ± 0.000015
T_{14}	Total transit duration (days)	0.1129 ± 0.0016	$0.1209^{+0.0045}_{-0.0030}$	$0.1431^{+0.0042}_{-0.0038}$
b	Transit Impact parameter	$0.59^{+0.10}_{-0.27}$	$0.720^{+0.041}_{-0.064}$	$0.729^{+0.064}_{-0.11}$
$\langle F \rangle$	Incident Flux (10^9 erg s^{-1} cm^{-2})	$1.347^{+0.085}_{-0.076}$	$0.697^{+0.040}_{-0.035}$	$0.295^{+0.018}_{-0.016}$

et al. 2006), and using broadband photometry to fit the SED following Stassun et al. (2018); both analyses yielded results consistent with the EXOFASTv2 fit.

4. False-positive Analysis

While experience from the *Kepler* mission has taught us that small planet candidates from space-based transit surveys are usually planets (Morton & Johnson 2011), especially those in multitransiting systems (Lissauer et al. 2012), careful analysis is required to rule out false-positive scenarios. During the *Kepler* and *K2* eras, it became common to "statistically validate" planet candidates using tools like `vespa` (Morton 2012, 2015), `BLENDER` (Torres et al. 2011), and `PASTIS` (Díaz et al. 2014) that quantify the likelihood that the any given signal arises from a false positive.

Planet candidates discovered by *TESS* often have advantages over candidates from *Kepler*/*K2*, which can make it possible to rule out some or all false-positive scenarios categorically, rather than calculating probabilities based on false-positive population models. In particular, most *TESS* planet candidates are observed at a 2 minute cadence, so we can precisely measure ingress/egress times, and many *TESS* targets are nearby and have high proper motion, so it is possible to show that background stars cannot cause the transit signals.

For HR 858, we take advantage of both approaches. We consider the following false-positive scenarios for one or more of the transit signals around HR 858:

1. *HR 858 is an eclipsing binary:* Our RV observations from MINERVA-Australis and TRES rule out this scenario (Section 2.3).
2. *Light from an unassociated eclipsing binary or transiting planet system is blended with HR 858:* If the transit signal comes from a star other than HR 858, the observed transit depth δ will be

$$\delta \simeq \left(\frac{R_{p,\mathrm{true}}}{R_\star}\right)^2 \frac{F_{\mathrm{source}}}{F_{\mathrm{total}}}, \tag{1}$$

where $R_{p,\mathrm{true}}/R_\star$ is the true radius ratio of the transiting/eclipsing body on the source star, and $F_{\mathrm{source}}/F_{\mathrm{total}}$ is the fraction of the flux the source star contributes to the *TESS* light curve. The ratio of the transit ingress/egress duration, t_{12}, to the duration from first to third contact ($t_{13} \equiv t_{14} - t_{12}$) constrains the radius ratio of the transit source regardless of any diluting flux (from Seager & Mallén-Ornelas 2003, Equation (21)):

$$\frac{R_{p,\mathrm{true}}}{R_\star} \leqslant \frac{t_{12}}{t_{13}}. \tag{2}$$

We calculate the magnitude difference Δm between HR 858 and the faintest companion that could cause the transit signals we see:

$$\delta \lesssim \left(\frac{t_{12}}{t_{13}}\right)^2 \frac{F_{\mathrm{source}}}{F_{\mathrm{total}}} \approx \left(\frac{t_{12}}{t_{13}}\right)^2 10^{-0.4\Delta m}, \tag{3}$$

$$\Delta m \lesssim 2.5 \log_{10}\left(\frac{t_{12}^2}{t_{13}^2 \delta}\right). \tag{4}$$

Using Equation (4) and our transit analysis (Section 3), we find $\Delta m \lesssim 4.5$, 5.9, and 6.1 mag for HR 858 b, c, and d, respectively (95% confidence). Analysis of the *TESS* image centroids shows that the source of the transits must be within 40″ of HR 858 (Section 2.1), and archival imaging (Section 2.2) shows no stars both close enough and bright enough to contribute the transit signals, including at HR 858's present-day position, ruling out background false-positive scenarios.

3. *Light from a physically associated companion that is an eclipsing binary or transiting planet system is blended with HR 858:* The comoving companion HR 858 B is too faint (*Gaia* Rp = 14.5, ΔRp = 8.6 mag) to contribute the transits based on our Δm constraints, and there is no evidence of any brighter resolved companions in speckle/archival imaging or any unresolved companion causing an RV acceleration. False-positive scenarios involving bound companions to HR 858 are therefore unlikely, but we cannot conclusively rule out the possibility that HR 858 has an undetected companion bright enough to contribute the transits.

Since we cannot rule out all false-positive scenarios involving physically associated companions to HR 858, we use `vespa` to evaluate the probability of these false-positive scenarios. Using the *TESS* light curve of each planet candidate and constraints from spectroscopy and imaging, `vespa` finds low false-positive probabilities (FPPs) for all three planet candidates (FPP $< 10^{-3}$ for each candidate), so we consider HR 858 b, c, and d to be validated planets.

5. Discussion

HR 858 is one of the brightest stars known to host transiting planets, trailing only HD 219134 (Motalebi et al. 2015), π Mensae (Huang et al. 2018a), and 55 Cancri (Winn et al. 2011). Transiting planets around stars this bright afford rich opportunities for detailed characterization, including mass measurements through precise RV observations, secondary eclipse spectroscopy with the *James Webb Space Telescope*,[44] and measurements of the alignment of the planetary orbits

[44] The `PandExo` tool predicts that NIRCam observations (with a grism and the F444W filter) of a single secondary eclipse of HR 858 b should yield an 11σ detection over the full bandpass and ≈30% precision in 100 nm spectral bins. Despite HR 858 being near *James Webb Space Telescope*'s bright limits, the simulated observing efficiency was 67% using the SUBGRISM64, frametime = 0.34 s readout mode, and the star did not saturate the detectors.

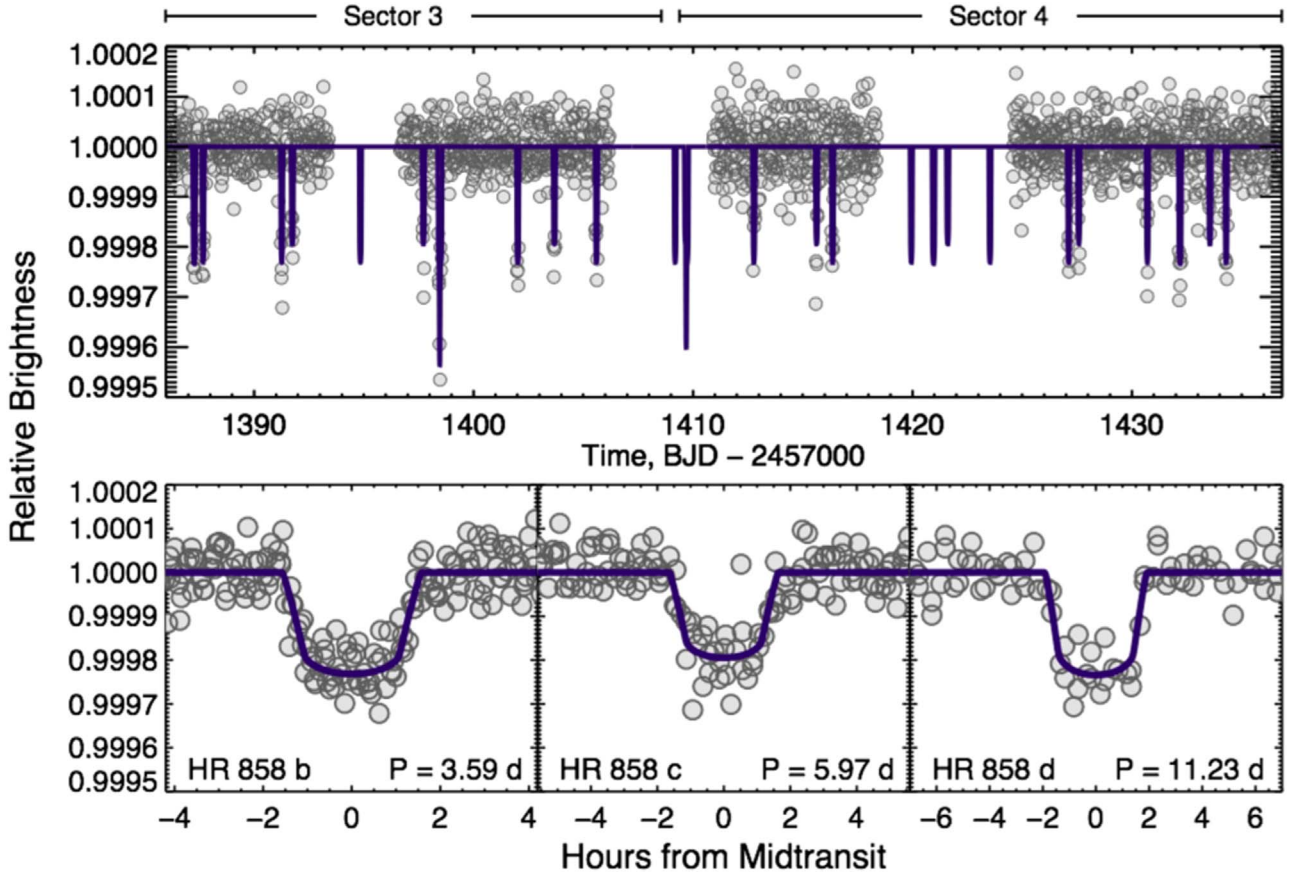

Figure 3. *TESS* light curves of HR 858. Top: full two-sector light curve. During Sector 3, *TESS* only downloaded images of HR 858 in its 30 minute cadence full-frame images (FFIs), but during Sector 4, HR 858 was preselected for observations at a 2 minute cadence. We bin the Sector 4 observations to an equivalent 30 minute cadence for visual clarity. Bottom: phase-folded *TESS* light curves of the three planets transiting HR 858, with the Sector 4 observations again binned to a 30 minute cadence for visual clarity. All analysis, including transit fitting, was performed on the unbinned 2 minute cadence Sector 4 light curve.

(The data used to create this figure are available.)

and stellar spin axis via the Rossiter–McLaughlin effect (McLaughlin 1924; Rossiter 1924) or Doppler Tomography.[45] HR 858 stands out even among the brightest known transiting systems because of its multiplicity; the next-brightest star known to host three transiting planets is nine times fainter than HR 858. (see Figure 4).

From *Kepler*, we know of many examples of compact, multitransiting, and coplanar systems, but relatively few of these systems are in true mean motion resonances (Fabrycky et al. 2014). The HR 858 system could be one of the exceptions to this rule; HR 858 b and c may be in a true 3:5 mean motion resonance. We assessed these planets' resonant state by randomly drawing 50 sets of initial orbital parameters from the EXOFASTv2 posterior probability distributions and performing *N*-body integrations for 10^5 yr using the `Mercury6` (Chambers 1999) code. We used a hybrid symplectic and Bulirsch–Stoer integrator, with a time step of 90 minutes and energy conservation kept to 1 part in 10^8 or better. The simulations include the stellar quadrupole field due to rotation as a J_2 moment, which we estimated to be $J_2 \approx 10^{-6}$ by modeling the star as an $n = 3$ polytrope (Lanza et al. 2011; Batygin & Adams 2013) with our derived mass/radius/rotational velocity. About one-third of the simulated system realizations show at least some evidence of mean motion resonance: 20% of the realizations exhibited librating resonance angles for the entire duration of the simulation, while another 14% exhibited librating resonance angles some of the time. Long-term RV and/or transit monitoring will help determine the resonant state of these planets; lower eccentricities for planets b and c[46] and weaker perturbations from the outer planet d[47] should make a resonance more likely.

The comoving stellar companion, HR 858 B, adds further intrigue to the system's architecture. The *Gaia* proper motion measurements for the primary and secondary differ by 13.9 ± 0.2 mas yr^{-1}. If we interpret this discrepancy as relative orbital motion between the two stars (and not systematics due to the large brightness contrast or unresolved orbital motion if HR 858 B is indeed itself a close binary), the orbit of HR 858 B about HR 858 A must be misaligned from the orbits of the

[45] Though HR 858's moderate rotation complicates RV observations, it is possible to measure precise RVs of even more rapidly rotating stars (Barros et al. 2017). Early RV observations of HR 858 indicate it is possible to achieve precision of a few m s^{-1} (D. Gandolfi and D. Anderson 2019, private communication), similar to the expected 1–2 m s^{-1} amplitude of the RV orbits and Rossiter–McLaughlin signals.

[46] The 3:5 mean motion resonance, in particular, is both easier to generate during disk migration (Quillen 2006) and more easily maintained in the presence of nearby planetary perturbers when the system eccentricities are low. A more narrow libration width, characteristic at lower eccentricities, presents fewer opportunities for a nearby perturbing planet to disrupt the resonance.

[47] In our simulations, we found evidence that lower masses and eccentricities for planet d increased the likelihood of planets b and c being in resonance.

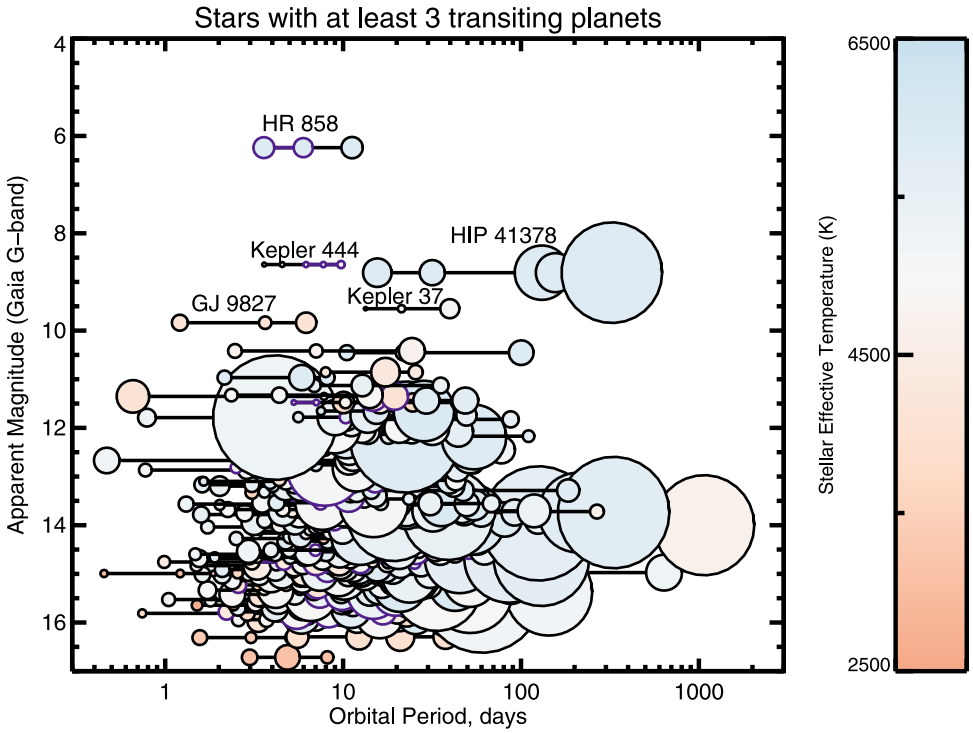

Figure 4. HR 858 in the context of other known transiting exoplanet systems. Shown plotted are all known systems with at least three transiting planets, as a function of the host stars' apparent brightness at visible wavelengths. The planets within each system are connected together with a horizontal line, and the planet radii and host star effective temperatures are encoded by the size and color of the symbols, respectively. We identified all pairs of planets within 1% of first-order (1:2, 2:3, 3:4, 4:5, 5:6, 6:7) mean motion resonances, and within 0.1% of second-order (1:3, 3:5, 5:7) mean motion resonances, and connected these planets together with purple lines. HR 858 stands out as the brightest of all known three-transiting-planet systems, while its compact near-resonant architecture is reminiscent of the population of compact multiplanet systems discovered by *Kepler*.

transiting system by at least 40°.[48] If true, HR 858 B could have torqued HR 858's planet-forming disk, causing a misalignment between the stellar spin axis and the transiting super-Earths' orbits. In particular, HR 858 B's mass and projected separation appear to put the system in a regime where the timescale for stellar spin axis realignment would be longer than the disk dissipation timescale, potentially "freezing in" the misalignment (Batygin 2012; Spalding & Batygin 2014). Future monitoring of the HR 858 A/B binary orbit should confirm its misalignment with the transit system and determine whether these mechanisms could create a spin/orbit misaligned multiplanetary system (that could be identified via Rossiter–McLaughlin observations of HR 858 b, c, or d).

Though the *TESS* prime mission survey is only about 25% complete, there may not be many new transiting planets around stars brighter than HR 858 left to discover. Prelaunch estimates of the *TESS* planet yield (Sullivan et al. 2015; Barclay et al. 2018; Huang et al. 2018b) predicted a handful of planet discoveries around naked-eye stars, and so far only HR 858 and π Mensae have fit this description. HR 858 will thus likely retain its privileged position as one of the brightest transit hosts in the sky and most favorable systems for detailed study.

We thank Jen Winters and Michael Fausnaugh for helpful discussions. We acknowledge the use of public *TESS* Alert data from pipelines at the *TESS* Science Office and at the *TESS* Science Processing Operations Center. Funding for the *TESS* mission is provided by NASA's Science Mission directorate. Resources supporting this work were provided by the NASA High-End Computing (HEC) Program through the NASA Advanced Supercomputing (NAS) Division at Ames Research Center for the production of the SPOC data products. AV's work was performed under contract with the California Institute of Technology/Jet Propulsion Laboratory funded by NASA through the Sagan Fellowship Program executed by the NASA Exoplanet Science Institute. C.X.H. and J.B. acknowledge support from MIT's Kavli Institute as Torres postdoctoral fellows. J.A.D. and J.N.W. acknowledge support from the Heising–Simons Foundation. J.E.R. is supported by the Harvard Future Faculty Leaders Postdoctoral fellowship. J.C.B is supported by the NSF Graduate Research Fellowship grants No. DGE 1256260 and a graduate fellowship from the Leinweber Center for Theoretical Physics. Some of the data presented in this paper were obtained from the Mikulski Archive for Space Telescopes (MAST). STScI is operated by the Association of Universities for Research in Astronomy, Inc., under NASA contract NAS5–26555. Support for MAST for non-HST data is provided by the NASA Office of Space Science via grant NNX13AC07G and by other grants and contracts. This work has made use of data from the European Space Agency (ESA) mission *Gaia* (https://www.cosmos.esa.int/gaia), processed by the *Gaia* Data Processing and Analysis Consortium (DPAC, https://www.cosmos.esa.int/web/gaia/dpac/consortium). Funding for the DPAC has been provided by national institutions, in particular the institutions participating in the *Gaia* Multilateral Agreement. MINERVA-Australis is supported by Australian Research Council LIEF grant LE160100001, Discovery grant DP180100972, Mount Cuba Astronomical Foundation, and institutional partners University

[48] As determined by a fit of the binary orbit using code available at https://github.com/logan-pearce/LOFTI (L. A. Pearce et al. 2019, in preparation).

of Southern Queensland, UNSW Australia, MIT, Nanjing University, George Mason University, University of Louisville, University of California Riverside, University of Florida, and University of Texas at Austin. This work makes use of observations from the LCOGT network. This research has made use of NASA's Astrophysics Data System and the NASA Exoplanet Archive, which is operated by the California Institute of Technology, under contract with the National Aeronautics and Space Administration under the Exoplanet Exploration Program. The National Geographic Society–Palomar Observatory Sky Atlas (POSS-I) was made by the California Institute of Technology with grants from the National Geographic Society. The Oschin Schmidt Telescope is operated by the California Institute of Technology and Palomar Observatory.

Facilities: TESS, FLWO:1.5 m (TRES), SOAR (HRCAM), LCO:1 m (NRES), ATT (echelle), CTIO:1.5 m (CHIRON).

Software: IDL Astronomy Library (Landsman 1993), EXOFASTv2 (Eastman et al. 2013; Eastman 2017), Mercury6 (Chambers 1999), vespa (Morton 2012, 2015), Orbits for the Impatient (Blunt et al. 2017, L. A. Pearce et al. 2019, in preparation), RadVel (Fulton et al. 2018), numpy (Oliphant 2006), pandas (McKinney et al. 2010), matplotlib (Hunter 2007), Pandexo (Batalha et al. 2017).

ORCID iDs

Andrew Vanderburg https://orcid.org/0000-0001-7246-5438
Chelsea X. Huang https://orcid.org/0000-0003-0918-7484
Juliette C. Becker https://orcid.org/0000-0002-7733-4522
David W. Latham https://orcid.org/0000-0001-9911-7388
Joshua N. Winn https://orcid.org/0000-0002-4265-047X
Jon M. Jenkins https://orcid.org/0000-0002-4715-9460
Allyson Bieryla https://orcid.org/0000-0001-6637-5401
Brendan P. Bowler https://orcid.org/0000-0003-2649-2288
Timothy M. Brown https://orcid.org/0000-0001-5062-0847
Christopher J. Burke https://orcid.org/0000-0002-7754-9486
Jennifer A. Burt https://orcid.org/0000-0002-0040-6815
Jason A. Dittmann https://orcid.org/0000-0001-7730-2240
Benjamin J. Fulton https://orcid.org/0000-0003-3504-5316
Jonathan Horner https://orcid.org/0000-0002-1160-7970
Stephen R. Kane https://orcid.org/0000-0002-7084-0529
Adam L. Kraus https://orcid.org/0000-0001-9811-568X
Laura Kreidberg https://orcid.org/0000-0003-0514-1147
Nicolas Law https://orcid.org/0000-0001-9380-6457
Andrew W. Mann https://orcid.org/0000-0003-3654-1602
Timothy D. Morton https://orcid.org/0000-0002-8537-5711
Logan A. Pearce https://orcid.org/0000-0003-3904-7378
Peter Plavchan https://orcid.org/0000-0002-8864-1667
Samuel N. Quinn https://orcid.org/0000-0002-8964-8377
Markus Rabus https://orcid.org/0000-0003-2935-7196
Avi Shporer https://orcid.org/0000-0002-1836-3120
Jeffrey C. Smith https://orcid.org/0000-0002-6148-7903
Keivan Stassun https://orcid.org/0000-0002-3481-9052
Rob Wittenmyer https://orcid.org/0000-0001-9957-9304
George Zhou https://orcid.org/0000-0002-4891-3517
Carl A. Ziegler https://orcid.org/0000-0002-0619-7639

References

Addison, B., Wright, D. J., Wittenmyer, R. A., et al. 2019, arXiv:1901.11231
Anglada-Escudé, G., & Butler, R. P. 2012, ApJS, 200, 15
Barclay, T., Pepper, J., & Quintana, E. V. 2018, ApJS, 239, 2
Barros, S. C. C., Gosselin, H., Lillo-Box, J., et al. 2017, A&A, 608, A25
Batalha, N. E., Mandell, A., Pontoppidan, K., et al. 2017, PASP, 129, 064501
Batygin, K. 2012, Natur, 491, 418
Batygin, K., & Adams, F. C. 2013, ApJ, 778, 169
Blunt, S., Nielsen, E. L., De Rosa, R. J., et al. 2017, AJ, 153, 229
Borucki, W. J., Koch, D., Basri, G., et al. 2010, Sci, 327, 977
Brown, T. M., Baliber, N., Bianco, F. B., et al. 2013, PASP, 125, 1031
Buchhave, L. A., Bizzarro, M., Latham, D. W., et al. 2014, Natur, 509, 593
Buchhave, L. A., Latham, D. W., Johansen, A., et al. 2012, Natur, 486, 375
Casagrande, L., Schönrich, R., Asplund, M., et al. 2011, A&A, 530, A138
Chambers, J. E. 1999, MNRAS, 304, 793
Choi, J., Dotter, A., Conroy, C., et al. 2016, ApJ, 823, 102
Claret, A., & Bloemen, S. 2011, A&A, 529, A75
da Silva, L., Girardi, L., Pasquini, L., et al. 2006, A&A, 458, 609
Díaz, R. F., Almenara, J. M., Santerne, A., et al. 2014, MNRAS, 441, 983
Dragomir, D., Teske, J., Gunther, M. N., et al. 2019, ApJL, 875, L7
Eastman, J. 2017, EXOFASTv2: Generalized Publication-quality Exoplanet Modeling Code, Astrophysics Source Code Library, ascl:1710.003
Eastman, J., Gaudi, B. S., & Agol, E. 2013, PASP, 125, 83
Eastman, J., Siverd, R., & Gaudi, B. S. 2010, PASP, 122, 935
Eastman, J. D., Brown, T. M., Hygelund, J., et al. 2014, Proc. SPIE, 9147, 914716
Evans, D. F. 2018, RNAAS, 2, 20
Fabrycky, D. C., Lissauer, J. J., Ragozzine, D., et al. 2014, ApJ, 790, 146
Fausnaugh, M. M., Vallely, P. J., Kochanek, C. S., et al. 2019, arXiv:1904.02171
Fressin, F., Torres, G., Charbonneau, D., et al. 2013, ApJ, 766, 81
Fulton, B. J., Petigura, E. A., Blunt, S., & Sinukoff, E. 2018, PASP, 130, 044504
Gaia Collaboration, Brown, A. G. A., Vallenari, A., et al. 2018, A&A, 616, A1
Gaia Collaboration, Prusti, T., de Bruijne, J. H. J., et al. 2016, A&A, 595, A1
Gontcharov, G. A. 2006, AstL, 32, 759
Gray, R. O., Corbally, C. J., Garrison, R. F., et al. 2006, AJ, 132, 161
Howell, S. B., Sobeck, C., Haas, M., et al. 2014, PASP, 126, 398
Huang, C. X., Burt, J., Vanderburg, A., et al. 2018a, ApJL, 868, L39
Huang, C. X., Shporer, A., Dragomir, D., et al. 2018b, arXiv:1807.11129
Hunter, J. D. 2007, CSE, 9, 90
Jenkins, J. M. 2015, BAAS, 3, 106.05
Jenkins, J. M., Caldwell, D. A., Chandrasekaran, H., et al. 2010, ApJL, 713, L120
Jenkins, J. M., Twicken, J. D., McCauliff, S., et al. 2016, Proc. SPIE, 9913, 99133E
Kovács, G., Zucker, S., & Mazeh, T. 2002, A&A, 391, 369
Kurucz, R. L. 1992, in IAU Symp. 149, The Stellar Populations of Galaxies, ed. B. Barbuy & A. Renzini (Dordrecht: Kluwer), 225
Landsman, W. B. 1993, in ASP Conf. Ser. 52, Astronomical Data Analysis Software and Systems II, ed. R. J. Hanisch, R. J. V. Brissenden, & J. Barnes (San Francisco, CA: ASP), 246
Lanza, A. F., Damiani, C., & Gandolfi, D. 2011, A&A, 529, A50
Lissauer, J. J., Fabrycky, D. C., Ford, E. B., et al. 2011, Natur, 470, 53
Lissauer, J. J., Marcy, G. W., Rowe, J. F., et al. 2012, ApJ, 750, 112
Mann, A. W., Gaidos, E., Vanderburg, A., et al. 2017, AJ, 153, 64
McKinney, W. 2010, in Proc. 9th Python in Science Conf. 445, ed. S. van der Walt & J. Millman, 51, http://conference.scipy.org/proceedings/scipy2010/mckinney.html
McLaughlin, D. B. 1924, ApJ, 60, 22
Morton, T. D. 2012, ApJ, 761, 6
Morton, T. D. 2015, VESPA: False Positive Probabilities Calculator, Astrophysics Source Code Library, ascl:1503.011
Morton, T. D., & Johnson, J. A. 2011, ApJ, 738, 170
Motalebi, F., Udry, S., Gillon, M., et al. 2015, A&A, 584, A72
Nielsen, L. D., Bouchy, F., Turner, O., et al. 2019, A&A, 623, A100
Oliphant, T. E. 2006, A Guide to NumPy (Spanish Fork, UT: Trelgol Publishing)
Petigura, E. A. 2015, PhD thesis, Univ. California
Petigura, E. A., Howard, A. W., Marcy, G. W., et al. 2017, AJ, 154, 107
Quillen, A. C. 2006, MNRAS, 365, 1367
Quinn, S. N., Becker, J. C., Rodriguez, J. E., et al. 2019, arXiv:1901.09092
Ricker, G. R., Winn, J. N., Vanderspek, R., et al. 2015, JATIS, 1, 014003
Rizzuto, A. C., Vanderburg, A., Mann, A. W., et al. 2018, AJ, 156, 195
Rodriguez, J. E., Quinn, S. N., Huang, C. X., et al. 2019, AJ, 157, 191
Rossiter, R. A. 1924, ApJ, 60, 15
Schlegel, D. J., Finkbeiner, D. P., & Davis, M. 1998, ApJ, 500, 525

Seager, S., & Mallén-Ornelas, G. 2003, ApJ, 585, 1038
Siverd, R. J., Brown, T. M., Barnes, S., et al. 2018, Proc. SPIE, 10702, 107026C
Siverd, R. J., Brown, T. M., Hygelund, J., et al. 2016, Proc. SPIE, 9908, 99086X
Smith, J. C., Stumpe, M. C., Van Cleve, J. E., et al. 2012, PASP, 124, 1000
Spalding, C., & Batygin, K. 2014, ApJ, 790, 42
Stassun, K. G., Corsaro, E., Pepper, J. A., & Gaudi, B. S. 2018, AJ, 155, 22
Stefanik, R. P., Latham, D. W., & Torres, G. 1999, in ASP Conf. Ser. 185, IAU Coll. 170, Precise Stellar Radial Velocities, ed. J. B. Hearnshaw & C. D. Scarfe (San Francisco, CA: ASP), 354
Stumpe, M. C., Smith, J. C., Catanzarite, J. H., et al. 2014, PASP, 126, 100
Sullivan, P. W., Winn, J. N., Berta-Thompson, Z. K., et al. 2015, ApJ, 809, 77
Tokovinin, A. 2018, PASP, 130, 035002
Torres, G., Fressin, F., Batalha, N. M., et al. 2011, ApJ, 727, 24
Vanderburg, A., & Johnson, J. A. 2014, PASP, 126, 948
Vanderburg, A., Latham, D. W., Buchhave, L. A., et al. 2016, ApJS, 222, 14
Vanderspek, R., Huang, C. X., Vanderburg, A., et al. 2019, ApJL, 871, L24
Wang, S., Jones, M., Shporer, A., et al. 2019, AJ, 157, 51
Winn, J. N., Matthews, J. M., Dawson, R. I., et al. 2011, ApJL, 737, L18
Zhou, G., Rodriguez, J. E., Vanderburg, A., et al. 2018, AJ, 156, 93